

SUPPLEMENTARY INFORMATION

Triple-cation perovskite solar cells fabricated by  
hybrid PVD/blade coating process using green  
solvents

*Severin Siegrist, Shih-Chi Yang, Evgeniia Gilshtein, Xiaoxiao Sun, Ayodhya N. Tiwari and Fan Fu\**

Laboratory for Thin Films and Photovoltaics, Empa – Swiss Federal Laboratories for Materials  
Science and Technology, Ueberlandstrasse 129, 8600 Duebendorf, Switzerland

\*Email: fan.fu@empa.ch

## EXPERIMENTAL SECTION

**Perovskite film by PVD/blade:** The inorganic halide template was sequentially deposited in a high-vacuum ( $< 6 \times 10^{-6}$  mbar), in-house developed thermal evaporator. First, 15 nm of CsI (> 99 %, TCI) was evaporated with 0.1 nm/s, followed by 300 nm of PbI<sub>2</sub> (> 99 %, TCI) with 0.7 nm/s. Next, the organic halide precursors, formamidinium iodide (FAI, > 99.99 %, greatcellsolar), methylammonium bromide (MABr, > 99.99 %, greatcellsolar) and methylammonium chloride (MACl, > 99.0 %, Sigma-Aldrich) were mixed according to FAI/MABr/MACl 60/6/6 mg in 1ml isopropanol. The mixed solution was blade coated with 30 mm/s at 65 °C and with a gap of 100 μm in ambient air, followed by 15 min annealing at 150 °C in ambient air (~ 35 % relative humidity).

**Perovskite film by Spin + Spin:** The inorganic halide template was deposited by spin coating 1.3 M of PbI<sub>2</sub> (> 99 %, TCI) and 0.065 M of CsI (> 99 %, TCI) dissolved in mixed N,N-dimethylformamide (DMF, 99.8 %, Sigma-Aldrich) and dimethyl sulfoxide (DMSO, ≥ 99.9 %) with volume ratio of 9:1 at 1500 r.p.m. for 30 s and annealed at 70 °C for 1 min inside the glovebox. Next, the organic halide precursors, formamidinium iodide (FAI, > 99.99 %, greatcellsolar), methylammonium bromide (MABr, > 99.99 %, greatcellsolar) and methylammonium chloride (MACl, > 99.0 %, Sigma-Aldrich) were mixed according to FAI/MABr/MACl 60/6/6 mg in 1ml isopropanol. The mixed solution was spin coated with 1300 r.p.m. for 40 s in the glovebox, followed by 15 min annealing at 150 °C in ambient air (~ 35 % relative humidity).

**Solar cell fabrication:** The solar cell was fabricated with a layer structure of IOH/SnO<sub>2</sub>/perovskite/PEAI/Spiro-OMeTAD/Au. First, hydrogenated indium oxide (IOH) with a sheet resistance of 10 Ω/sq were deposited on cleaned soda-lime glass substrates in a high-vacuum sputtering system (CT200, Allianceconcept) by RF sputtering of ceramic In<sub>2</sub>O<sub>3</sub> targets (99.99 %,

10 in. diameter, SPM AG) in a mixed Ar, O<sub>2</sub>, and H<sub>2</sub> atmosphere at room temperature according to Yang et al.<sup>1</sup>. Afterwards, the IOH film was annealed at 200 °C for 20 min in ambient air (35 - 40 % rel. humidity). Oxygen plasma treatment was performed for 5 min on the substrate before blade coating the electron transporting layer (ETL). SnO<sub>2</sub> colloid precursor (15 wt% in H<sub>2</sub>O colloidal dispersion, Alfa Aesar) was diluted in de-ionized water 1:3 by volume and blade coated with 30 mm/s at 70 °C and a gap between blade and substrate of 100 µm in ambient air. The SnO<sub>2</sub> was annealed at 150 °C for 30 min in ambient air. The perovskite with thickness around 560 nm was deposited on top of the ETL via one of the indicated two-step fabrication methods. After perovskite formation, 5 mg of phenethylammonium iodide (PEAI, 98 %, Sigma-Aldrich) per ml of isopropanol was spin coated onto the perovskite film with a spin rate of 5000 r.p.m. Next, the hole transporting layer Spiro-OMeTAD layer was blade coated with 90 mm/s at 40 °C and with a gap of 100 µm in ambient air on top of perovskite layer with a solution that contained 25 mg 2,2',7,7'-tetrakis-(N,N'-di-p-methoxyphenylamine)-9,9'-spirobifluorene (Xi'an Polymer Light Technology), 10 µl of 4-tert-butylpyridine (98 %, Sigma-Aldrich) and 6 µl of lithium bis(trifluoromethanesulfonyl)imide (Li-TFSI) solution (520 mg of Li-TFSI (99 %, Sigma-Aldrich) in 1 ml of acetonitrile (99.8 %, Sigma-Aldrich)) in 1 ml of p-Xylene ( $\geq$  99 %, Sigma-Aldrich). Finally, 80 nm Au back electrode was thermally evaporated with 0.15 nm/s at a base pressure of  $< 6 \times 10^{-6}$  mbar.

**Solar cell performance characterizations:** Photocurrent–voltage (J–V) characteristics were measured in four-contact mode at standard test conditions (100 mWcm<sup>-2</sup>) using a Keithley 2400 source meter. A solar simulator (ABA class, LOT-QuantumDesign) was calibrated using a certified monocrystalline silicon solar cell (RS-ID-5, Fraunhofer-ISE) and was used to simulate the AM 1.5 G one sun illumination. Illumination is in superstrate configuration without external

cooling of the sample. The active area is 0.1 cm<sup>2</sup> of each pixel, defined by the mask of the gold electrode. The J–V measurements were performed in both forward (from -0.2 to 1.2 V) and backward (from 1.2 to -0.2 V) directions in ambient air (~40 % relative humidity) at room temperature. No pretreatment, e.g., bias or illumination, was applied before measurement. The steady-state efficiency as a function of time was recorded using a maximum power point tracker, which adjusts the applied voltage in order to reach the maximum power point (perturb and observe algorithm). The external quantum efficiency of the devices were measured with a lock-in amplifier. The probing beam was generated by a chopped white source (900W, halogen lamp, 280 Hz) and a dual grating monochromator. The beam size was adjusted to ensure that the illumination area was fully inside the cell area. A certified single crystalline silicon solar cell was used as a reference cell. White light bias was applied during the measurement with ~ 0.1 sun intensity.

## Material characterizations

**ToF-SIMS:** Element depth profiles were obtained with a time-of-flight secondary ion mass spectrometer (ToF.SIMS V system, ION-TOF). The primary beam was 25 keV Bi<sup>3+</sup> with a total current of 0.22 pA and a raster size of 50 × 50 μm<sup>2</sup>. For detection of negative ions, Cs<sup>+</sup> ions were used with 500 eV ion energy, 25 nA pulse current on a 300 × 300 μm<sup>2</sup> raster size to bombard and etch the film. For detection of positive ions, sputtering was performed using O<sub>2</sub><sup>-</sup> ions at 2 keV ion energy, 180 nA pulse current over a raster size of 300 × 300 μm<sup>2</sup>. The data were plotted with the intensity for each signal normalized to the total counts of the signal.

**XPS.** X-ray photoelectron spectroscopy was performed using a Quantum 2000 system from Physical Electronics with a monochromatic Al K<sub>α</sub>source (1486.6 eV, spot size, 100 μm) and a base pressure below 8 × 10<sup>-8</sup> mbar. No surface cleaning was performed. Detailed high-resolution scans

of I 3d, S 2p, N 1s, Cl 2p, O 1s, Br 3d, C 1s, Cs 3d, Pb 4f were recorded with an energy step size of 0.125 eV and a pass energy of 29.35 eV during depth profile sputtering by Ar<sup>+</sup> sputtering. The first five cycles (with the first measurement performed directly on the surface) were performed with 0.5 kV energy after 30 s sputtering each, followed by five more cycles: three with 2 min intervals and 2 more with 4 min intervals with the same energy. The sputtering rate was estimated to be around 15-20 nm/min which corresponds to 250-300 nm total depth of the performed analysis. With the use of MultiPak processing software all data were background subtracted.

**TRPL/PL:** Time-resolved photoluminescence (TRPL) and steady-state photoluminescence (PL) were measured using a FluoTime 300 unit coupled into a MicroTime 100 system from PicoQuant. For TRPL measurement, a 639 nm pulsed laser with < 100 ps pulse width was used as an excitation source. The spot size was measured using a NanoScan2 beam profiler resulting in ~ 130 mm diameter. The excitation was  $3 \times 10^{11}$  photons cm<sup>-2</sup> pulse<sup>-1</sup> and the pulse frequency was 0.1 MHz. For the fitting procedure, a bi-exponential decay was used and the first 20 ns after the signal peak were neglected.

**AFM:** The AFM characterization was carried out using an AFM microscope (Bruker ICON3) in the air. A silicon nitride tip (ScanAsyst-air) with a radius of 10 nm was used as the probe. The cantilevers' spring constant and resonant frequency are 0.4 N/m and 70 kHz, respectively.

**UV-Vis:** Reflectance and transmittance measurements were performed using a Shimadzu UV-Vis 3600 spectrophotometer equipped with an integrating sphere. The reflectance data were corrected for the instrumental response stemming from diffuse and specular reflections both on the sample, and the reflectance measurements were carried out in a wavelength range from 300 to 1500 nm.

**XRD:** X-Ray diffraction patterns were measured on an X'Pert Pro in Bragg–Brentano geometry using Cu K<sub>α1</sub> radiation ( $\lambda = 1.5406 \text{ \AA}$ ), scanning from 5 to 60 ° (2θ) with a step interval of 0.0167°.

**SEM:** The SEM micrographs were taken with a Hitachi S-4800 Scanning Electron Microscope using 5–10 kV acceleration voltage. A thin layer (1 nm) of Pt was coated on top of the samples to avoid charging effects.

## NOTES

### **Note S1: Morphology of inorganic halide template with different amorphous substrates**

Fu et al. have shown that the crystal characteristics of the substrate influence the morphology of the evaporated inorganic template <sup>2</sup>. While amorphous substrates yield in compact PbI<sub>2</sub> layers, poly-crystalline substrates lead to porous, plate-like PbI<sub>2</sub> layers. We use this finding to deposit perovskite films on amorphous substrates to avoid further material restrictions for the perovskite fabrication method by PVD/blade. We provide SEM cross-section images of the inorganic halide template on different amorphous materials, including a) soda-lime glass (SLG), b) IOH and c) colloidal SnO<sub>2</sub> nanocrystals to support the versatility of this method. As depicted in **Figure S16c-d**, the morphology of the evaporated inorganic halide template is similar for each of these substrates and in all cases, we obtain a compact inorganic template. Additionally, the XRD spectra of these films show a comparable crystallinity of the evaporated inorganic template with a preferred orientation of (001) plane over (101) (**Figure S16a**). Therefore, we assume a similar infiltration mechanism for the organic halide precursor solution into the inorganic halide template. Hence, we expect a comparable perovskite film formation by PVD/blade for any amorphous substrate, including inert quartz.

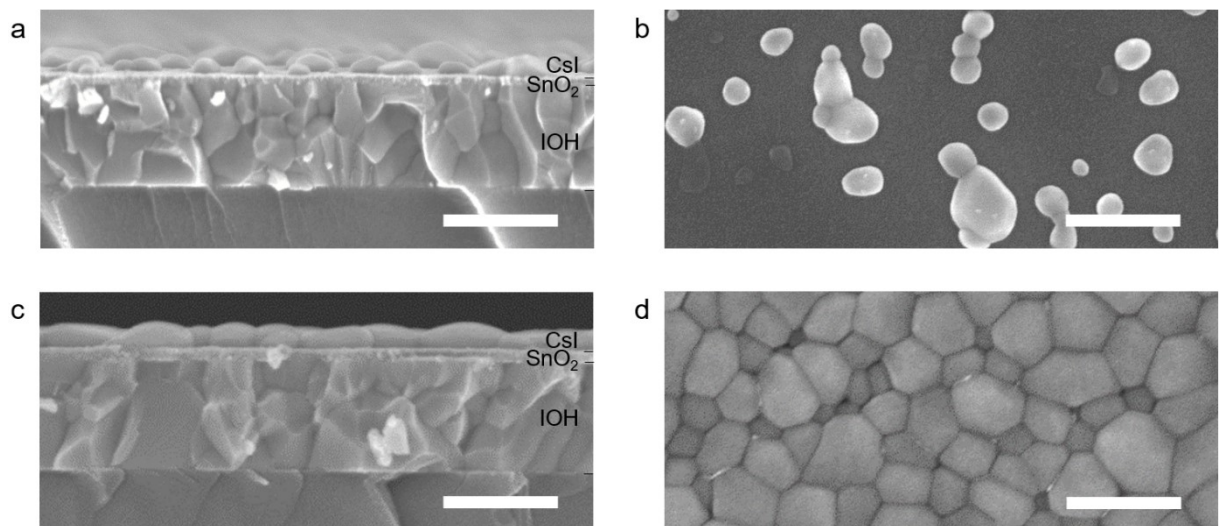


Figure S1: SEM cross-section and top view images of 15 nm (a, b) and 100 nm (c, d) CsI evaporated on top of SnO<sub>2</sub>. The hygroscopic nature of CsI leads to the formation of islands. Covering CsI with sufficiently thick PbI<sub>2</sub> layer conserves a uniform CsI layer and prevents it from forming islands. The scale bar is 500 nm.

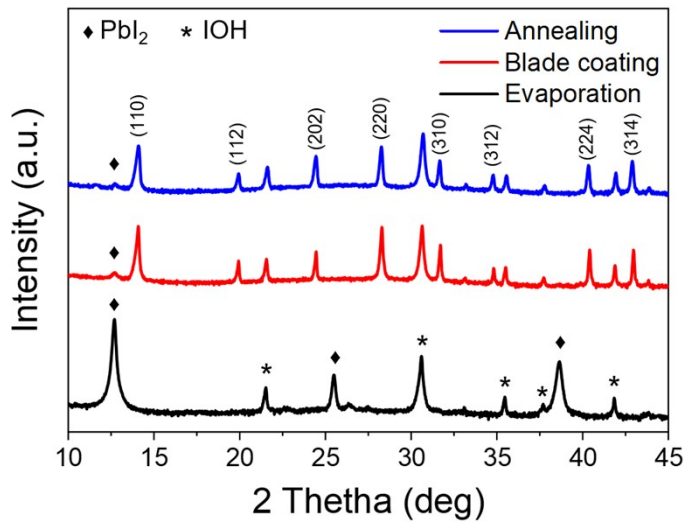


Figure S2: XRD patterns (log-scale) of the film after thermal evaporation, blade coating and annealing with indicated perovskite crystal plane orientations.  $\text{PbI}_2$  is labeled by  $\blacklozenge$  and IOH by \*.

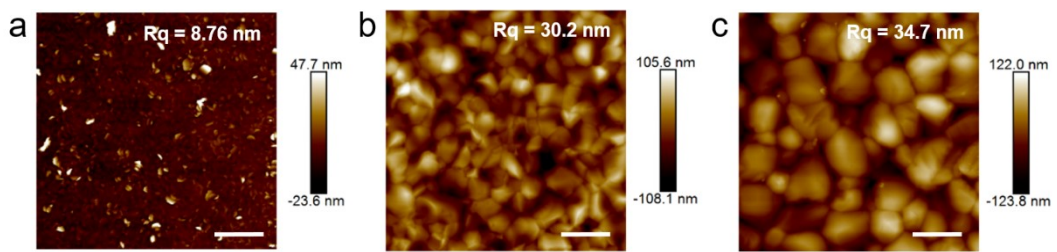


Figure S3: AFM height images of the film surface after a) evaporation, b) blade coating and c) annealing. The scale bar is 1  $\mu\text{m}$ .

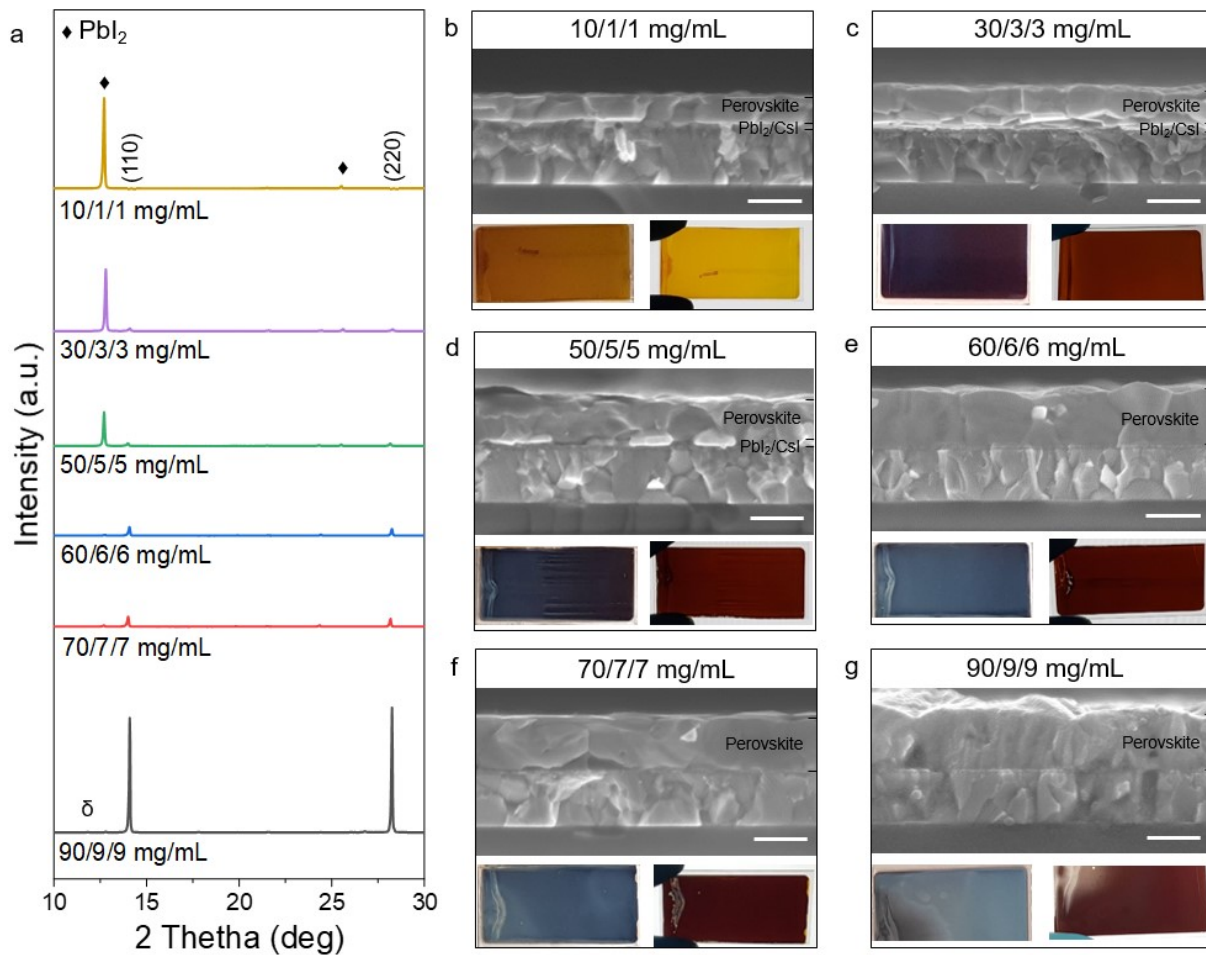


Figure S4: Perovskite films fabricated with different concentrations of the organic halide precursors (FAI/MABr/MACl in mg/mL) in the solution. a) XRD pattern with indicated diffraction peaks of the  $\alpha$ -phase perovskite crystal planes. The  $\delta$ -phase perovskite is labeled by  $\delta$  and  $\text{PbI}_2$  by  $\blacklozenge$ . b-g) SEM cross-section view images for each concentration with sample pictures taken in foreground and in background illumination mode. The scale bar is 500 nm.

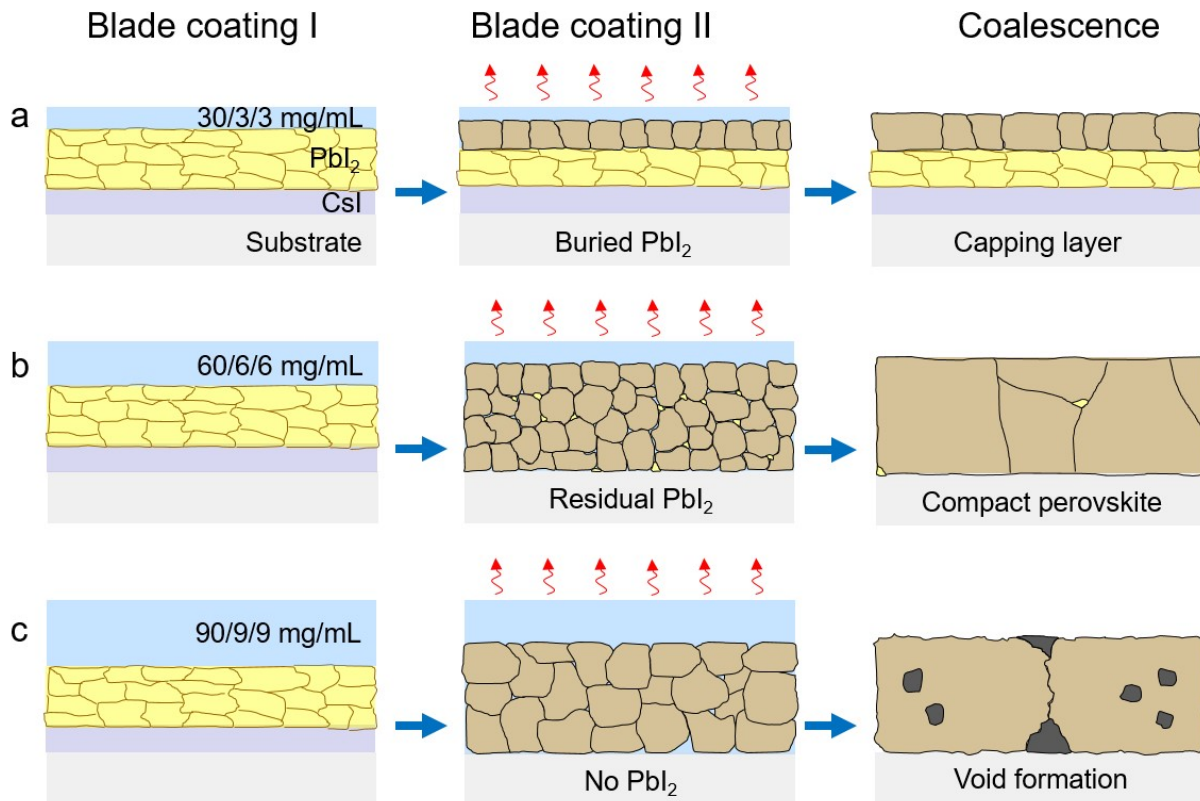


Figure S5: Influence of organic halide precursor concentration on the degree of perovskite conversion of the film. a) Formation of perovskite capping layer when blade coating of  $30/3/3$  mg/mL FAI/MABr/MACl on the inorganic halide template. b) Almost fully converted perovskite film with unreacted  $\text{PbI}_2$  residues for  $60/6/6$  mg/mL. c) Formation of defective, but highly crystalline perovskite film with voids in the bulk and rough crystal grains, when using  $90/9/9$  mg/mL of organic halide precursors. The amount of organic halide precursors is represented by the solution thickness (blue).

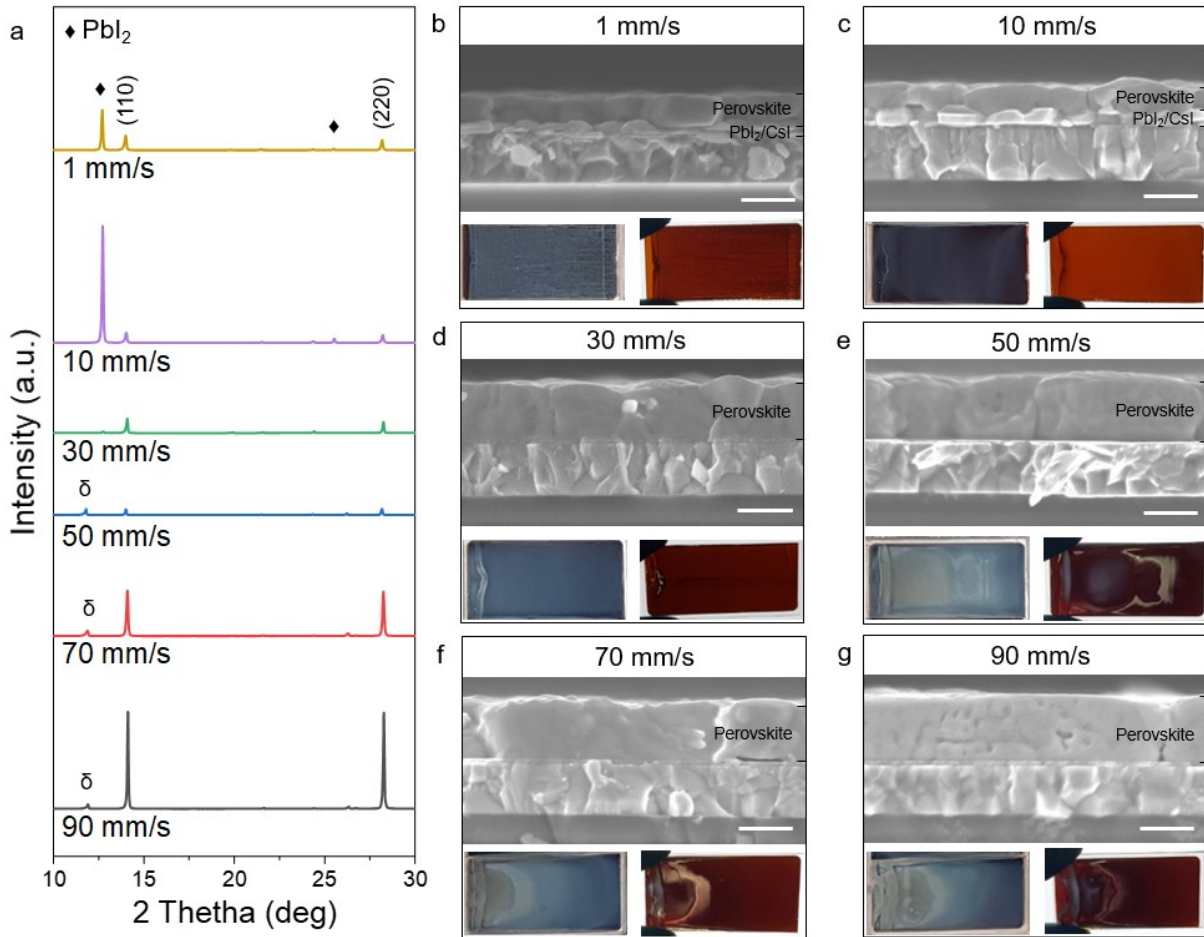


Figure S6: Perovskite films fabricated with different blading speeds. a) XRD pattern with indicated diffraction peaks of the  $\alpha$ -phase perovskite crystal planes. The  $\delta$ -phase perovskite is labeled by  $\delta$  and  $\text{PbI}_2$  by  $\blacklozenge$ . b-g) SEM cross-section view images for each speed with sample pictures taken in foreground and in background illumination mode. The scale bar is 500 nm.

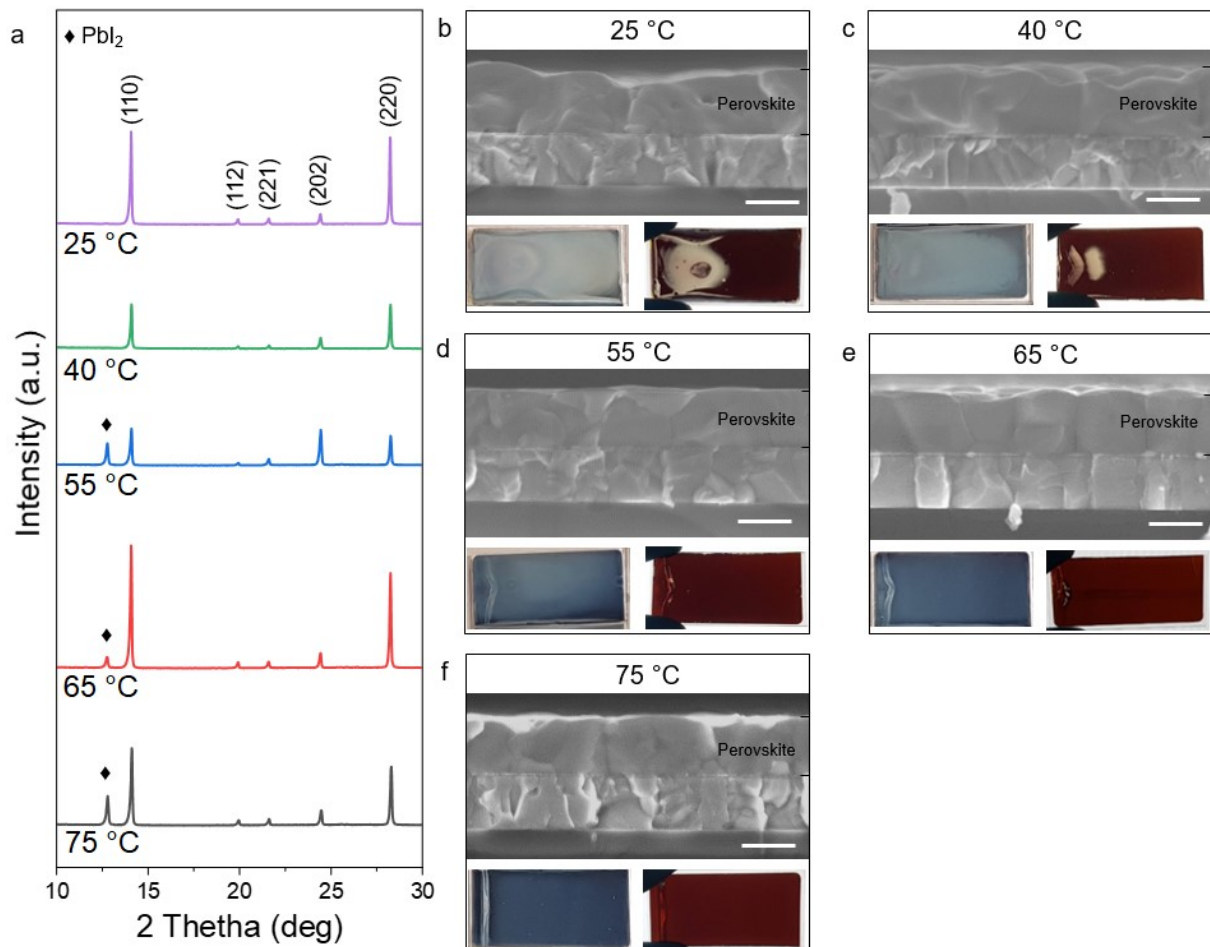


Figure S7: Perovskite films fabricated at different substrate temperatures. a) XRD pattern with indicated diffraction peaks of the  $\alpha$ -phase perovskite crystal planes. PbI<sub>2</sub> is labeled by  $\blacklozenge$ . b-f) SEM cross-section view images for each substrate temperature with sample pictures taken in foreground and in background illumination mode. The scale bar is 500 nm.

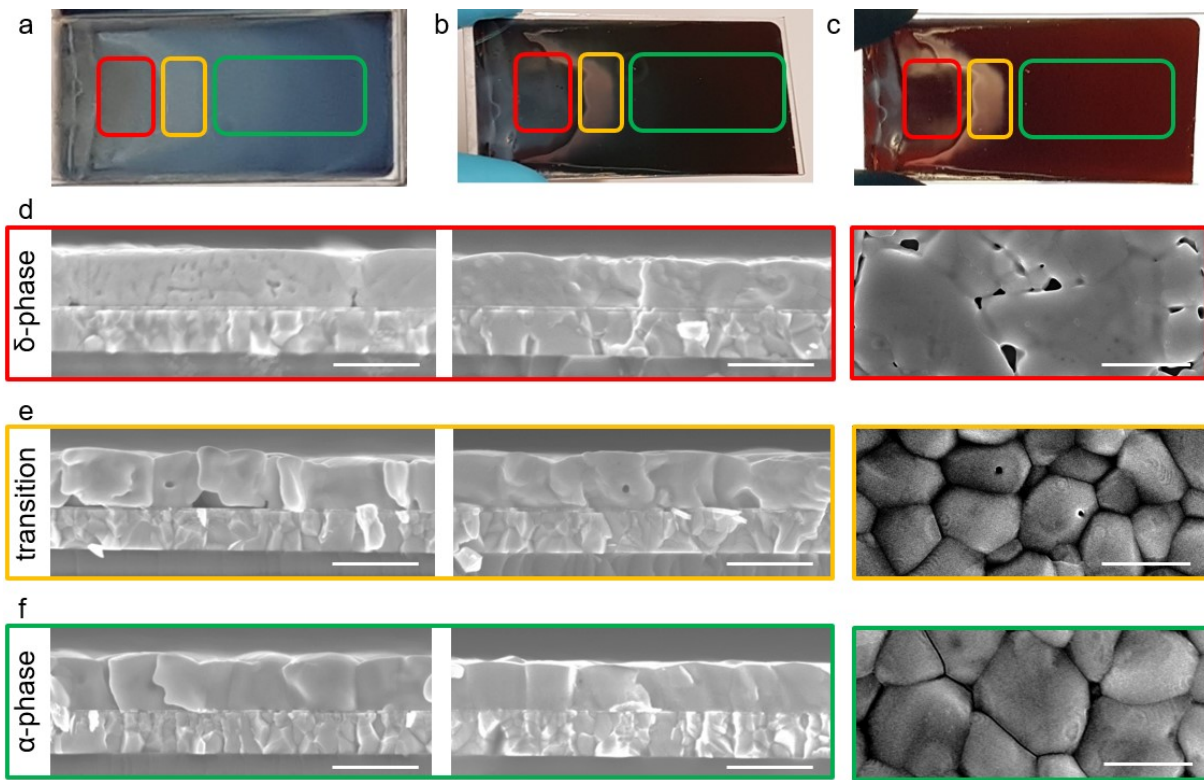


Figure S8: Perovskite crystal phases and morphology that occur, when the processing parameters are not matching, i.e. the balance of inorganic halide precursors and organic halide precursors is not given. Sample pictures of the perovskite film blade coated with 70 mm/s at 65 °C with an organic halide concentration of 60/6/6 mg/mL of FAI/MABr/MACl in foreground illumination mode: a) front side and b) backside of the sample as well as in c) background illumination mode. SEM cross-section and top view images of the d)  $\delta$ -phase perovskite region, e) transition region and f)  $\alpha$ -phase perovskite region. The scale bar is 1  $\mu\text{m}$ .

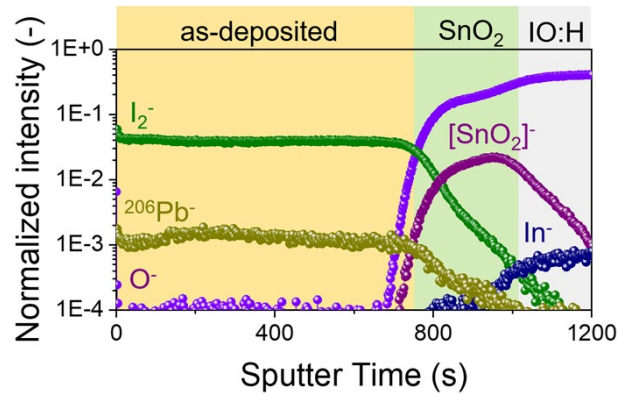


Figure S9: ToF-SIMS depth profile of negative species of the as-deposited film.

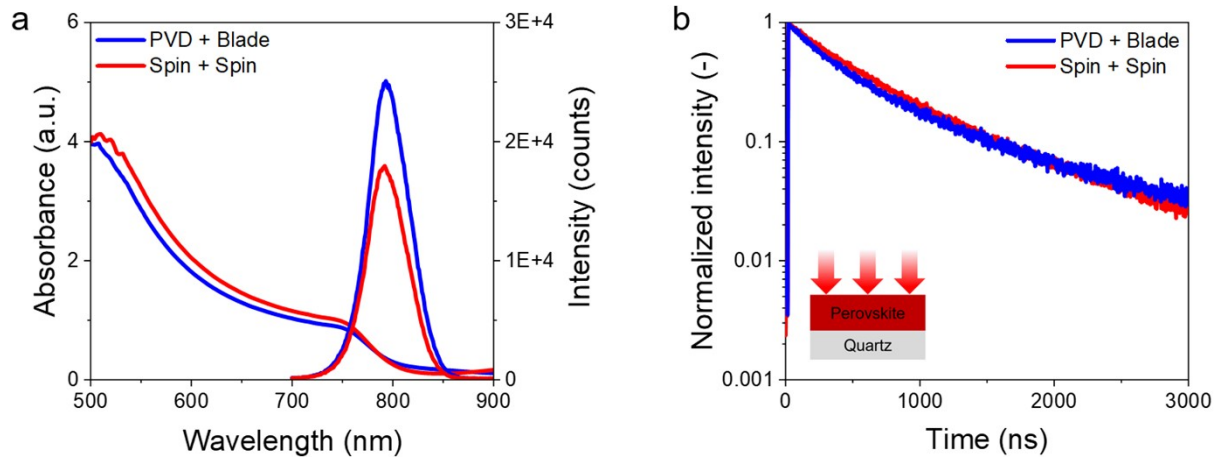


Figure S10: Optoelectronic properties of perovskite films fabricated by the PVD/blade process (PVD + Blade) and by two-step spin coating (Spin + Spin) on quartz. a) Ultraviolet-visible (UV-Vis) absorbance and photoluminescence (PL) spectra, b) time-resolved photoluminescence (TRPL) decays. The decay lifetimes are obtained by fitting the measurement with the bi-exponential decay function

$$I(t) = A_1 \exp\left(-\frac{t}{\tau_1}\right) + A_2 \exp\left(-\frac{t}{\tau_2}\right)$$

The fitting parameters are provided in Table S1.

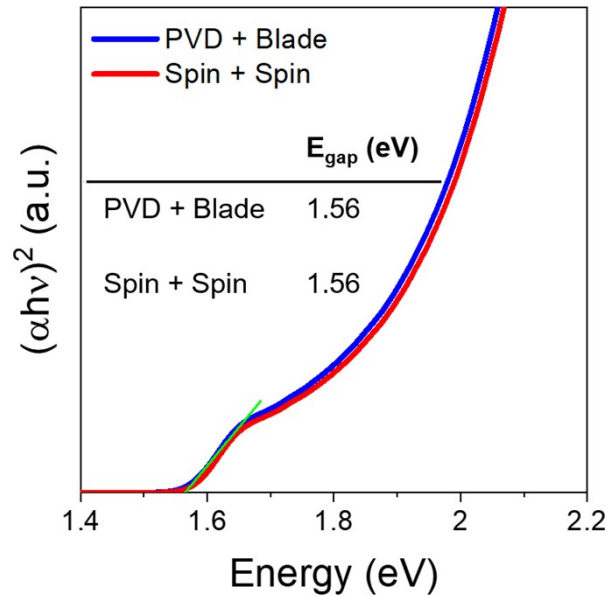


Figure S11: Tauc plot as a function of  $(\alpha h v)^2$  versus energy of the perovskite films by the PVD/blade process (PVD + Blade) and by two-step spin coating (Spin + Spin) on quartz. The extracted bandgap energy is 1.56 eV for both methods.

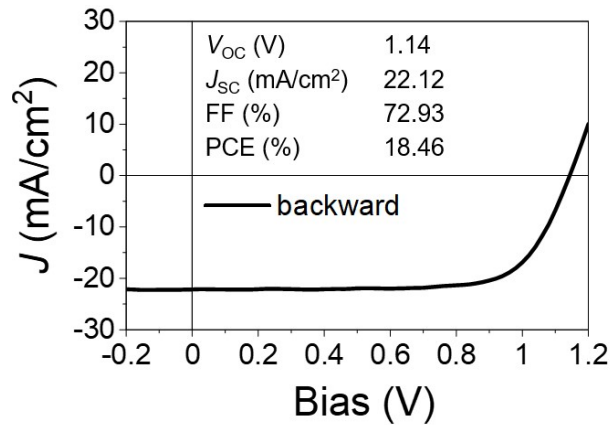


Figure S12: Photovoltaic performance of PSC with two-step spin coated perovskite absorber layer (Spin + Spin) and blade coated charge transporting layers.

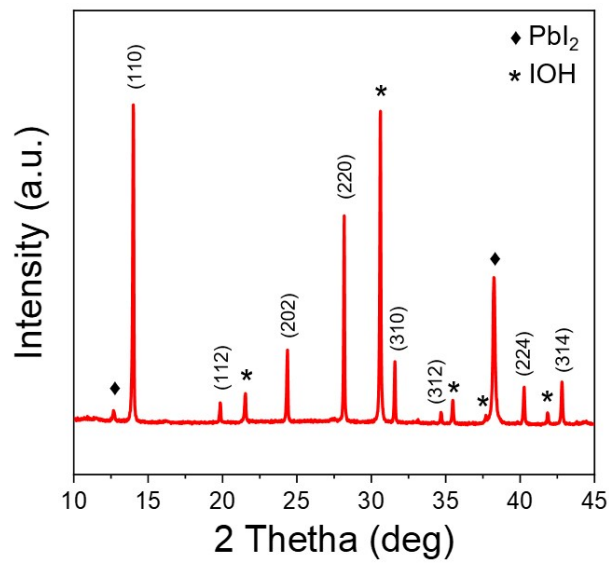


Figure S13: XRD pattern of PSC device. Perovskite crystal planes are indexed.  $\text{PbI}_2$  is labeled by  $\blacklozenge$  and IOH by \*.

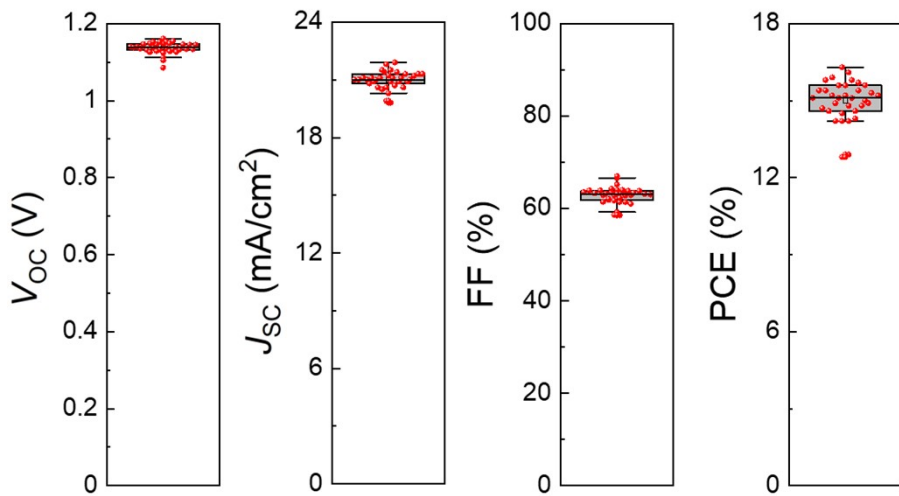


Figure S14: Photovoltaic performance overview of 36 PSC devices on 5 cm x 5 cm sample with blade coated charge transporting layers and perovskite fabricated by PVD/blade process.

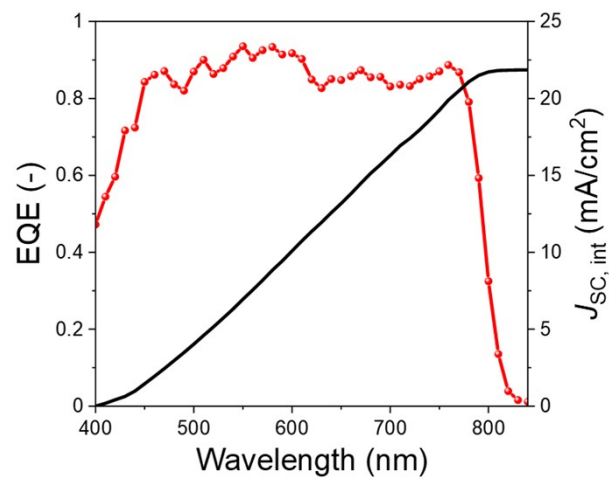


Figure S15: EQE spectrum with integrated  $J_{SC}$  value of 21.86 mA/cm<sup>2</sup> for the PSC device.

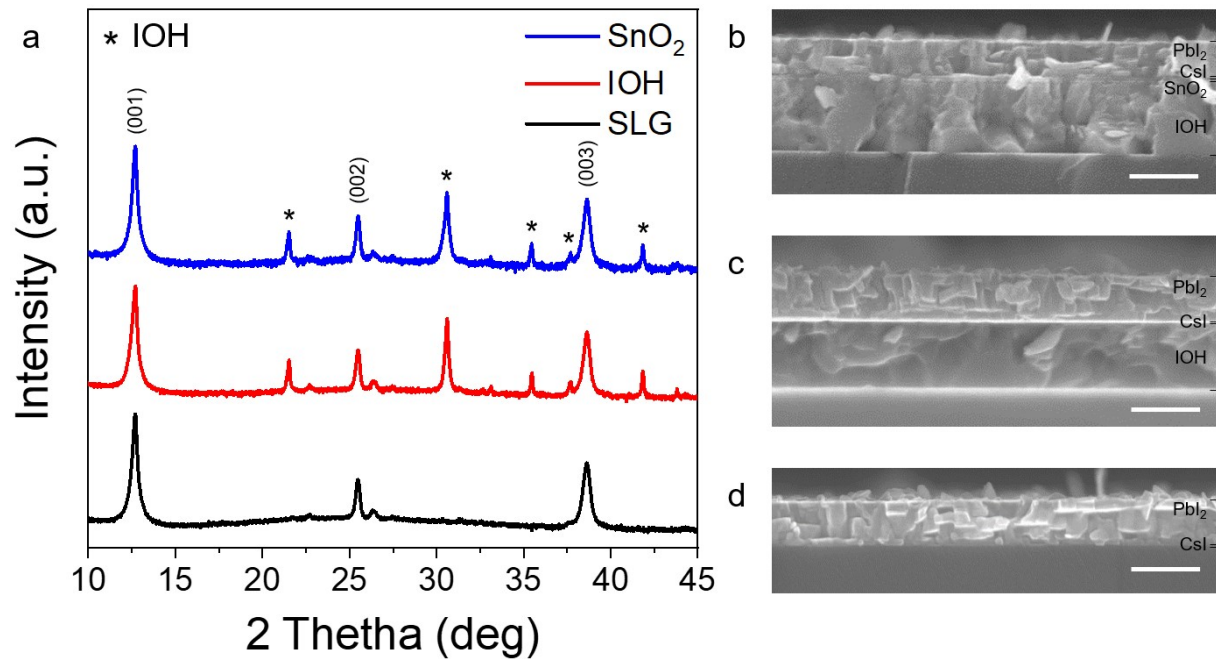


Figure S16: XRD patterns of the inorganic halide template ( $\text{PbI}_2/\text{CsI}$ ), sequentially evaporated on  $\text{SnO}_2$  (blue), on IOH (red) and on soda-lime glass (SLG, black). a)  $\text{PbI}_2$  crystal planes are indexed and IOH is labeled by \*. Corresponding SEM cross-section view images of the inorganic halide template on b)  $\text{SnO}_2$ , c) IOH and d) SLG. The scale bar is 500 nm.

Table S1: Fitting parameters of the bi-exponential decay function of the time-resolved photoluminescence (TRPL) measurement of the perovskite films obtained by PVD/blade process and by two-step spin coating. Average decay time  $\tau$  was calculated according to: 
$$\tau = \frac{A_1\tau_1 + A_2\tau_2}{A_1 + A_2}$$
<sup>3</sup>.

Method	$A_1$	$\tau_1$ (ns)	$A_2$	$\tau_2$ (ns)	$\tau$ (ns)
PVD + Blade	2094.29	342.52	737.74	1405.7	619.48
Spin + Spin	3107.67	395.59	1603.44	1148.4	651.81

Table S2: Summary of the chart in Figure 4d with selected work of perovskite solar cells with indicated layers fabricated by scalable deposition methods.

YEAR	SCALABLE LAYERS	PCE	STACK	REF
2019	PVK	20.2	FTO/SnO <sub>2</sub> /PVK/Spiro-OMeTAD/Ag	<sup>4</sup>
2020	PVK	19.6	FTO/SnO <sub>2</sub> /PVK/Spiro-OMeTAD/Au	<sup>5</sup>
2020	PVK	20.3	ITO/SnO <sub>2</sub> /PCBM/PVK/Spiro-OMeTAD/Au	<sup>6</sup>
2021	PVK	20.6	ITO/MeO-2PACz/PVK/PCBM/BCP/Ag	<sup>7</sup>
2016	PVK/ETL	18.3	FTO/c-TiO <sub>2</sub> /PVKPTAA/Au	<sup>8</sup>
2016	PVK/ETL	15.6	FTO/c-TiO <sub>2</sub> /m-TiO <sub>2</sub> /PVK/Spiro-OMeTAD/Au	<sup>9</sup>
2017	PVK/ETL	20.1	FTO/TiO <sub>2</sub> /PVK/PTAA/Ag	<sup>10</sup>
2017	PVK/ETL	16.6	FTO/c-TiO <sub>2</sub> /PVK/Spiro-OMeTAD/Au	<sup>11</sup>
2017	PVK/ETL	18.6	FTO/c-TiO <sub>2</sub> /m-TiO <sub>2</sub> /PVK/Spiro-OMeTAD/Au	<sup>4</sup>
2017	PVK/ETL	15.8	FTO/C60/PVK/Spiro-OMeTAD/Ag	<sup>12</sup>
2018	PVK/ETL	17.3	FTO/SnO <sub>2</sub> /PVK/Spiro-OMeTAD/Au	<sup>13</sup>
2018	PVK/ETL	18.7	ITO/TiO <sub>2</sub> /PVK/Spiro-OMeTAD/Au	<sup>14</sup>
2020	PVK/ETL	20.6	ITO/MeO-2PACz/PVK/C60/BCP/Cu	<sup>15</sup>
2015	PVK/ETL/HTL	13.3	FTO/c-TiO <sub>2</sub> /m-TiO <sub>2</sub> /PVK/P3HT/Au	<sup>16</sup>
2017	PVK/ETL/HTL	14.0	FTO/c-TiO <sub>2</sub> /m-TiO <sub>2</sub> /m-ZrO <sub>2</sub> /PVK/Carbon	<sup>17</sup>
2018	PVK/ETL/HTL	20.3	ITO/PTAA/PVK/C60/BCP/Cu	<sup>18</sup>
2018	PVK/ETL/HTL	19.4	FTO/c-TiO <sub>2</sub> /PVK/Spiro-OMeTAD/Au	<sup>19</sup>
2018	PVK/ETL/HTL	16.8	FTO/c-TiO <sub>2</sub> /PVK/Spiro-OMeTAD/Au	<sup>20</sup>
2020	PVK/ETL/HTL	17.8	ITO/SnO <sub>2</sub> /SAM/PVK/PDCBT/Ta-WO <sub>x</sub> /Ag	<sup>21</sup>
2020	PVK/ETL/HTL	21.7	FTO/TiO <sub>2</sub> /PVK/PCBM/Ag	<sup>22</sup>
2020	PVK/ETL/HTL	16.3	ITO/SnO <sub>2</sub> /PVK/Spiro-OMeTAD/Au	<sup>23</sup>
2021	PVK/ETL/HTL	23.6	ITO/PTAA/PVK/C60/BCP/Cu	<sup>24</sup>

<b>2021</b>	PVK/ETL/HTL	18.9	FTO/TiO <sub>2</sub> /PVK/MoO <sub>3</sub> /NPB/Au	25
<b>2021</b>	PVK/ETL/HTL	23.2	ITO/PTAA/PVK/C60/BCP/Cu	26
<b>2021</b>	PVK/ETL/HTL	18.7	IOH/SnO <sub>2</sub> /PVK/Spiro-OMeTAD/Au	This work
<b>2021</b>	PVK/ETL/HTL	15.9	FTO/c-TiO <sub>2</sub> /mp-TiO <sub>2</sub> /PVK/Spiro-OMeTAD/Ag	27
<b>2021</b>	PVK/ETL/HTL	19.4	ITO/SnO <sub>2</sub> /PVK/HTL/Ta-WO <sub>x</sub> /Au	28
<b>2021</b>	PVK/ETL/HTL	16.1	TCO/CuPc/PVK/C60/BCP/Ag	29

## REFERENCES of Table S2

- (1) Jiang, Y.; Feurer, T.; Carron, R.; Sevilla, G. T.; Moser, T.; Pisoni, S.; Erni, R.; Rossell, M. D.; Ochoa, M.; Hertwig, R.; Tiwari, A. N.; Fu, F. High-Mobility In<sub>2</sub>O<sub>3</sub>:H Electrodes for Four-Terminal Perovskite/CuInSe<sub>2</sub>Tandem Solar Cells. *ACS Nano* **2020**, 14 (6), 7502–7512. <https://doi.org/10.1021/acsnano.0c03265>.
- (2) Fu, F.; Kranz, L.; Yoon, S.; Löckinger, J.; Jäger, T.; Perrenoud, J.; Feurer, T.; Gretener, C.; Buecheler, S.; Tiwari, A. N. Controlled Growth of PbI<sub>2</sub> Nanoplates for Rapid Preparation of CH<sub>3</sub>NH<sub>3</sub>PbI<sub>3</sub> in Planar Perovskite Solar Cells. *Phys. Status Solidi Appl. Mater. Sci.* **2015**, 212 (12), 2708–2717. <https://doi.org/10.1002/pssa.201532442>.
- (3) Liu, K.; Liang, Q.; Qin, M.; Shen, D.; Yin, H.; Ren, Z.; Zhang, Y.; Zhang, H.; Fong, P. W. K.; Wu, Z.; Huang, J.; Hao, J.; Zheng, Z.; So, S. K.; Lee, C. S.; Lu, X.; Li, G. Zwitterionic-Surfactant-Assisted Room-Temperature Coating of Efficient Perovskite Solar Cells. *Joule* **2020**, 4 (11), 2404–2425. <https://doi.org/10.1016/j.joule.2020.09.011>.
- (4) Yang, M.; Li, Z.; Reese, M. O.; Reid, O. G.; Kim, D. H.; Siol, S.; Klein, T. R.; Yan, Y.; Berry, J. J.; Van Hest, M. F. A. M.; Zhu, K. Perovskite Ink with Wide Processing Window for Scalable High-Efficiency Solar Cells. *Nat. Energy* **2017**, 2 (5), 1–9. <https://doi.org/10.1038/nenergy.2017.38>.
- (5) Lim, K. S.; Lee, D. K.; Lee, J. W.; Park, N. G. 17% Efficient Perovskite Solar Mini-Module: Via Hexamethylphosphoramide (HMPA)-Adduct-Based Large-Area D-Bar Coating. *J. Mater. Chem. A* **2020**, 8 (18), 9345–9354. <https://doi.org/10.1039/d0ta02017f>.
- (6) Li, J.; Wang, H.; Chin, X. Y.; Dewi, H. A.; Vergeer, K.; Goh, T. W.; Lim, J. W. M.; Lew, J. H.; Loh, K. P.; Soci, C.; Sum, T. C.; Bolink, H. J.; Mathews, N.; Mhaisalkar, S.; Bruno, A. Highly Efficient Thermally Co-Evaporated Perovskite Solar Cells and Mini-Modules. *Joule* **2020**, 4 (5), 1035–1053. <https://doi.org/10.1016/j.joule.2020.03.005>.
- (7) Li, J.; Dewi, H. A.; Wang, H.; Zhao, J.; Tiwari, N.; Yantara, N.; Malinauskas, T.; Getautis, V.; Savenije, T. J.; Mathews, N.; Mhaisalkar, S.; Bruno, A. Co-Evaporated MAPbI<sub>3</sub> with Graded Fermi Levels Enables Highly Performing, Scalable, and Flexible p-i-n Perovskite Solar Cells. *Adv. Funct. Mater.* **2021**, 2103252, 1–11. <https://doi.org/10.1002/adfm.202103252>.
- (8) Heo, J. H.; Lee, M. H.; Jang, M. H.; Im, S. H. Highly Efficient CH<sub>3</sub>NH<sub>3</sub>PbI<sub>3</sub>–xC<sub>x</sub>I Mixed Halide Perovskite Solar Cells Prepared by Re-Dissolution and Crystal Grain Growth via Spray Coating. *J. Mater. Chem. A* **2016**, 4 (45), 17636–17642. <https://doi.org/10.1039/c6ta06718b>.
- (9) Leyden, M. R.; Jiang, Y.; Qi, Y. Chemical Vapor Deposition Grown Formamidinium Perovskite Solar

- Modules with High Steady State Power and Thermal Stability. *J. Mater. Chem. A* **2016**, *4* (34), 13125–13132. <https://doi.org/10.1039/c6ta04267h>.
- (10) He, M.; Li, B.; Cui, X.; Jiang, B.; He, Y.; Chen, Y.; O’Neil, D.; Szymanski, P.; El-Sayed, M. A.; Huang, J.; Lin, Z. Meniscus-Assisted Solution Printing of Large-Grained Perovskite Films for High-Efficiency Solar Cells. *Nat. Commun.* **2017**, *8* (May). <https://doi.org/10.1038/ncomms16045>.
  - (11) Jiang, Y.; Leyden, M. R.; Qiu, L.; Wang, S.; Ono, L. K.; Wu, Z.; Juarez-Perez, E. J.; Qi, Y. Combination of Hybrid CVD and Cation Exchange for Upscaling Cs-Substituted Mixed Cation Perovskite Solar Cells with High Efficiency and Stability. *Adv. Funct. Mater.* **2018**, *28* (1). <https://doi.org/10.1002/adfm.201703835>.
  - (12) Borchert, J.; Milot, R. L.; Patel, J. B.; Davies, C. L.; Wright, A. D.; Martínez Maestro, L.; Snaith, H. J.; Herz, L. M.; Johnston, M. B. Large-Area, Highly Uniform Evaporated Formamidinium Lead Triiodide Thin Films for Solar Cells. *ACS Energy Lett.* **2017**, *2* (12), 2799–2804. <https://doi.org/10.1021/acsenergylett.7b00967>.
  - (13) Luo, L.; Zhang, Y.; Chai, N.; Deng, X.; Zhong, J.; Huang, F.; Peng, Y.; Ku, Z.; Cheng, Y. B. Large-Area Perovskite Solar Cells with  $\text{Cs}_x\text{FA}_1-x\text{PbI}_3-y\text{Br}_y$  Thin Films Deposited by a Vapor-Solid Reaction Method. *J. Mater. Chem. A* **2018**, *6* (42), 21143–21148. <https://doi.org/10.1039/c8ta06557h>.
  - (14) Li, J.; Munir, R.; Fan, Y.; Niu, T.; Liu, Y.; Zhong, Y.; Yang, Z.; Tian, Y.; Liu, B.; Sun, J.; Smilgies, D. M.; Thoroddsen, S.; Amassian, A.; Zhao, K.; Liu, S. (Frank). Phase Transition Control for High-Performance Blade-Coated Perovskite Solar Cells. *Joule* **2018**, *2* (7), 1313–1330. <https://doi.org/10.1016/j.joule.2018.04.011>.
  - (15) Roß, M.; Gil-Escríg, L.; Al-Ashouri, A.; Tockhorn, P.; Jošt, M.; Rech, B.; Albrecht, S. Co-Evaporated p-i-n Perovskite Solar Cells beyond 20% Efficiency: Impact of Substrate Temperature and Hole-Transport Layer. *ACS Appl. Mater. Interfaces* **2020**, *12* (35), 39261–39272. <https://doi.org/10.1021/acsami.0c10898>.
  - (16) Razza, S.; Di Giacomo, F.; Matteocci, F.; Cinà, L.; Palma, A. L.; Casaluci, S.; Cameron, P.; D’Epifanio, A.; Licoccia, S.; Reale, A.; Brown, T. M.; Di Carlo, A. Perovskite Solar Cells and Large Area Modules (100 Cm<sup>2</sup>) Based on an Air Flow-Assisted PbI<sub>2</sub> Blade Coating Deposition Process. *J. Power Sources* **2015**, *277*, 286–291. <https://doi.org/10.1016/j.jpowsour.2014.12.008>.
  - (17) Hu, Y.; Si, S.; Mei, A.; Rong, Y.; Liu, H.; Li, X.; Han, H. Stable Large-Area (10 × 10 Cm<sup>2</sup>) Printable Mesoscopic Perovskite Module Exceeding 10% Efficiency. *Sol. RRL* **2017**, *1* (2), 2–7. <https://doi.org/10.1002/solr.201600019>.
  - (18) Deng, Y.; Zheng, X.; Bai, Y.; Wang, Q.; Zhao, J.; Huang, J. Surfactant-Controlled Ink Drying Enables High-Speed Deposition of Perovskite Films for Efficient Photovoltaic Modules. *Nat. Energy* **2018**, *3* (7), 560–566. <https://doi.org/10.1038/s41560-018-0153-9>.
  - (19) Yang, M.; Kim, D. H.; Klein, T. R.; Li, Z.; Reese, M. O.; Tremolet De Villers, B. J.; Berry, J. J.; Van Hest, M. F. A. M.; Zhu, K. Highly Efficient Perovskite Solar Modules by Scalable Fabrication and Interconnection Optimization. *ACS Energy Lett.* **2018**, *3* (2), 322–328. <https://doi.org/10.1021/acsenergylett.7b01221>.
  - (20) Di Giacomo, F.; Shanmugam, S.; Fledderus, H.; Bruijnaers, B. J.; Verhees, W. J. H.; Dorenkamper, M. S.; Veenstra, S. C.; Qiu, W.; Gehlhaar, R.; Merckx, T.; Aernouts, T.; Andriessen, R.; Galagan, Y. Up-Scalable Sheet-to-Sheet Production of High Efficiency Perovskite Module and Solar Cells on 6-in. Substrate Using Slot Die Coating. *Sol. Energy Mater. Sol. Cells* **2018**, *181* (August 2017), 53–59. <https://doi.org/10.1016/j.solmat.2017.11.010>.
  - (21) Yang, F.; Dong, L.; Jang, D.; Tam, K. C.; Zhang, K.; Li, N.; Guo, F.; Li, C.; Arrive, C.; Bertrand, M.; Brabec, C. J.; Egelhaaf, H. J. Fully Solution Processed Pure  $\alpha$ -Phase Formamidinium Lead Iodide Perovskite Solar Cells for Scalable Production in Ambient Condition. *Adv. Energy Mater.* **2020**, *10* (42), 1–11. <https://doi.org/10.1002/aenm.202001869>.

- (22) Du, M.; Zhu, X.; Wang, L.; Wang, H.; Feng, J.; Jiang, X.; Cao, Y.; Sun, Y.; Duan, L.; Jiao, Y.; Wang, K.; Ren, X.; Yan, Z.; Pang, S.; Liu, S. High-Pressure Nitrogen-Extraction and Effective Passivation to Attain Highest Large-Area Perovskite Solar Module Efficiency. *Adv. Mater.* **2020**, *32* (47), 1–10. <https://doi.org/10.1002/adma.202004979>.
- (23) Bishop, J. E.; Read, C. D.; Smith, J. A.; Routledge, T. J.; Lidzey, D. G. Fully Spray-Coated Triple-Cation Perovskite Solar Cells. *Sci. Rep.* **2020**, *10* (1), 1–8. <https://doi.org/10.1038/s41598-020-63674-5>.
- (24) Chen, S.; Dai, X.; Xu, S.; Jiao, H.; Zhao, L.; Huang, J. Stabilizing Perovskite-Substrate Interfaces for High-Performance Perovskite Modules. *Science* (80-. ). **2021**, *373* (6557), 902 LP – 907. <https://doi.org/10.1126/science.abi6323>.
- (25) Feng, J.; Jiao, Y.; Wang, H.; Zhu, X.; Sun, Y.; Du, M.; Cao, Y.; Yang, D.; Liu, S. (Frank). High-Throughput Large-Area Vacuum Deposition for High-Performance Formamidine-Based Perovskite Solar Cells. *Energy Environ. Sci.* **2021**, *14* (5), 3035–3043. <https://doi.org/10.1039/d1ee00634g>.
- (26) Chen, S.; Xiao, X.; Gu, H.; Huang, J. Iodine Reduction for Reproducible and High-Performance Perovskite Solar Cells and Modules. **2021**, 1–7. <https://doi.org/10.1126/sciadv.abe8130>.
- (27) Adugna, G. B.; Abate, S. Y.; Wu, W. T.; Tao, Y. T. Toward Large-Area and Fully Solution-Sheared Perovskite Solar Cells. *ACS Appl. Mater. Interfaces* **2021**. <https://doi.org/10.1021/acsami.1c03460>.
- (28) Yang, F.; Dong, L.; Jang, D.; Saparov, B.; Tam, K. C.; Zhang, K.; Li, N.; Brabec, C. J.; Egelhaaf, H. J. Low Temperature Processed Fully Printed Efficient Planar Structure Carbon Electrode Perovskite Solar Cells and Modules. *Adv. Energy Mater.* **2021**, *2101219*. <https://doi.org/10.1002/aenm.202101219>.
- (29) Seto, S. Inverted Planer Perovskite Solar Cells Fabricated by All Vapor Phase Process. *Jpn. J. Appl. Phys.* **2021**, *60*, 0–6. <https://doi.org/10.35848/1347-4065/abdad3>.

## REFERENCES

- (1) Jiang, Y.; Feurer, T.; Carron, R.; Sevilla, G. T.; Moser, T.; Pisoni, S.; Erni, R.; Rossell, M. D.; Ochoa, M.; Hertwig, R.; Tiwari, A. N.; Fu, F. High-Mobility In<sub>2</sub>O<sub>3</sub>:H Electrodes for Four-Terminal Perovskite/CuInSe<sub>2</sub>Tandem Solar Cells. *ACS Nano* **2020**, *14* (6), 7502–7512. <https://doi.org/10.1021/acsnano.0c03265>.
- (2) Fu, F.; Kranz, L.; Yoon, S.; Löckinger, J.; Jäger, T.; Perrenoud, J.; Feurer, T.; Gretener, C.; Buecheler, S.; Tiwari, A. N. Controlled Growth of PbI<sub>2</sub> Nanoplates for Rapid Preparation of CH<sub>3</sub>NH<sub>3</sub>PbI<sub>3</sub> in Planar Perovskite Solar Cells. *Phys. Status Solidi Appl. Mater. Sci.* **2015**, *212* (12), 2708–2717. <https://doi.org/10.1002/pssa.201532442>.
- (3) Liu, K.; Liang, Q.; Qin, M.; Shen, D.; Yin, H.; Ren, Z.; Zhang, Y.; Zhang, H.; Fong, P. W. K.; Wu, Z.; Huang, J.; Hao, J.; Zheng, Z.; So, S. K.; Lee, C. S.; Lu, X.; Li, G. Zwitterionic-Surfactant-Assisted Room-Temperature Coating of Efficient Perovskite Solar Cells. *Joule* **2020**, *4* (11), 2404–2425. <https://doi.org/10.1016/j.joule.2020.09.011>.
- (4) Yang, M.; Li, Z.; Reese, M. O.; Reid, O. G.; Kim, D. H.; Siol, S.; Klein, T. R.; Yan, Y.; Berry, J. J.; Van Hest, M. F. A. M.; Zhu, K. Perovskite Ink with Wide Processing Window for Scalable High-Efficiency Solar Cells. *Nat. Energy* **2017**, *2* (5), 1–9. <https://doi.org/10.1038/nenergy.2017.38>.
- (5) Lim, K. S.; Lee, D. K.; Lee, J. W.; Park, N. G. 17% Efficient Perovskite Solar Mini-Module: Via Hexamethylphosphoramide (HMPA)-Adduct-Based Large-Area D-Bar Coating. *J. Mater. Chem. A* **2020**, *8* (18), 9345–9354. <https://doi.org/10.1039/d0ta02017f>.
- (6) Li, J.; Wang, H.; Chin, X. Y.; Dewi, H. A.; Vergeer, K.; Goh, T. W.; Lim, J. W. M.; Lew, J.

- H.; Loh, K. P.; Soci, C.; Sum, T. C.; Bolink, H. J.; Mathews, N.; Mhaisalkar, S.; Bruno, A. Highly Efficient Thermally Co-Evaporated Perovskite Solar Cells and Mini-Modules. *Joule* **2020**, *4* (5), 1035–1053. <https://doi.org/10.1016/j.joule.2020.03.005>.
- (7) Li, J.; Dewi, H. A.; Wang, H.; Zhao, J.; Tiwari, N.; Yantara, N.; Malinauskas, T.; Getautis, V.; Savenije, T. J.; Mathews, N.; Mhaisalkar, S.; Bruno, A. Co-Evaporated MAPbI<sub>3</sub> with Graded Fermi Levels Enables Highly Performing, Scalable, and Flexible p-i-n Perovskite Solar Cells. *Adv. Funct. Mater.* **2021**, *2103252*, 1–11. <https://doi.org/10.1002/adfm.202103252>.
- (8) Heo, J. H.; Lee, M. H.; Jang, M. H.; Im, S. H. Highly Efficient CH<sub>3</sub>NH<sub>3</sub>PbI<sub>3</sub>–xCl<sub>x</sub> Mixed Halide Perovskite Solar Cells Prepared by Re-Dissolution and Crystal Grain Growth via Spray Coating. *J. Mater. Chem. A* **2016**, *4* (45), 17636–17642. <https://doi.org/10.1039/c6ta06718b>.
- (9) Leyden, M. R.; Jiang, Y.; Qi, Y. Chemical Vapor Deposition Grown Formamidinium Perovskite Solar Modules with High Steady State Power and Thermal Stability. *J. Mater. Chem. A* **2016**, *4* (34), 13125–13132. <https://doi.org/10.1039/c6ta04267h>.
- (10) He, M.; Li, B.; Cui, X.; Jiang, B.; He, Y.; Chen, Y.; O’Neil, D.; Szymanski, P.; Ei-Sayed, M. A.; Huang, J.; Lin, Z. Meniscus-Assisted Solution Printing of Large-Grained Perovskite Films for High-Efficiency Solar Cells. *Nat. Commun.* **2017**, *8* (May). <https://doi.org/10.1038/ncomms16045>.
- (11) Jiang, Y.; Leyden, M. R.; Qiu, L.; Wang, S.; Ono, L. K.; Wu, Z.; Juarez-Perez, E. J.; Qi, Y. Combination of Hybrid CVD and Cation Exchange for Upscaling Cs-Substituted Mixed Cation Perovskite Solar Cells with High Efficiency and Stability. *Adv. Funct. Mater.* **2018**,

28 (1). <https://doi.org/10.1002/adfm.201703835>.

- (12) Borchert, J.; Milot, R. L.; Patel, J. B.; Davies, C. L.; Wright, A. D.; Martínez Maestro, L.; Snaith, H. J.; Herz, L. M.; Johnston, M. B. Large-Area, Highly Uniform Evaporated Formamidinium Lead Triiodide Thin Films for Solar Cells. *ACS Energy Lett.* **2017**, *2* (12), 2799–2804. <https://doi.org/10.1021/acsenergylett.7b00967>.
- (13) Luo, L.; Zhang, Y.; Chai, N.; Deng, X.; Zhong, J.; Huang, F.; Peng, Y.; Ku, Z.; Cheng, Y. B. Large-Area Perovskite Solar Cells with  $\text{Cs}_x\text{FA}_{1-x}\text{PbI}_3-y\text{Br}_y$  Thin Films Deposited by a Vapor-Solid Reaction Method. *J. Mater. Chem. A* **2018**, *6* (42), 21143–21148. <https://doi.org/10.1039/c8ta06557h>.
- (14) Li, J.; Munir, R.; Fan, Y.; Niu, T.; Liu, Y.; Zhong, Y.; Yang, Z.; Tian, Y.; Liu, B.; Sun, J.; Smilgies, D. M.; Thoroddsen, S.; Amassian, A.; Zhao, K.; Liu, S. (Frank). Phase Transition Control for High-Performance Blade-Coated Perovskite Solar Cells. *Joule* **2018**, *2* (7), 1313–1330. <https://doi.org/10.1016/j.joule.2018.04.011>.
- (15) Roß, M.; Gil-Escríg, L.; Al-Ashouri, A.; Tockhorn, P.; Jošt, M.; Rech, B.; Albrecht, S. Co-Evaporated p-i-n Perovskite Solar Cells beyond 20% Efficiency: Impact of Substrate Temperature and Hole-Transport Layer. *ACS Appl. Mater. Interfaces* **2020**, *12* (35), 39261–39272. <https://doi.org/10.1021/acsami.0c10898>.
- (16) Razza, S.; Di Giacomo, F.; Matteocci, F.; Cinà, L.; Palma, A. L.; Casaluci, S.; Cameron, P.; D’Epifanio, A.; Licoccia, S.; Reale, A.; Brown, T. M.; Di Carlo, A. Perovskite Solar Cells and Large Area Modules (100 Cm<sup>2</sup>) Based on an Air Flow-Assisted PbI<sub>2</sub> Blade Coating Deposition Process. *J. Power Sources* **2015**, *277*, 286–291. <https://doi.org/10.1016/j.jpowsour.2014.12.008>.

- (17) Hu, Y.; Si, S.; Mei, A.; Rong, Y.; Liu, H.; Li, X.; Han, H. Stable Large-Area ( $10 \times 10$  Cm<sup>2</sup>) Printable Mesoscopic Perovskite Module Exceeding 10% Efficiency. *Sol. RRL* **2017**, *1* (2), 2–7. <https://doi.org/10.1002/solr.201600019>.
- (18) Deng, Y.; Zheng, X.; Bai, Y.; Wang, Q.; Zhao, J.; Huang, J. Surfactant-Controlled Ink Drying Enables High-Speed Deposition of Perovskite Films for Efficient Photovoltaic Modules. *Nat. Energy* **2018**, *3* (7), 560–566. <https://doi.org/10.1038/s41560-018-0153-9>.
- (19) Yang, M.; Kim, D. H.; Klein, T. R.; Li, Z.; Reese, M. O.; Tremolet De Villers, B. J.; Berry, J. J.; Van Hest, M. F. A. M.; Zhu, K. Highly Efficient Perovskite Solar Modules by Scalable Fabrication and Interconnection Optimization. *ACS Energy Lett.* **2018**, *3* (2), 322–328. <https://doi.org/10.1021/acsenergylett.7b01221>.
- (20) Di Giacomo, F.; Shanmugam, S.; Fledderus, H.; Bruijnaers, B. J.; Verhees, W. J. H.; Dorenkamper, M. S.; Veenstra, S. C.; Qiu, W.; Gehlhaar, R.; Merckx, T.; Aernouts, T.; Andriessen, R.; Galagan, Y. Up-Scalable Sheet-to-Sheet Production of High Efficiency Perovskite Module and Solar Cells on 6-in. Substrate Using Slot Die Coating. *Sol. Energy Mater. Sol. Cells* **2018**, *181* (August 2017), 53–59. <https://doi.org/10.1016/j.solmat.2017.11.010>.
- (21) Yang, F.; Dong, L.; Jang, D.; Tam, K. C.; Zhang, K.; Li, N.; Guo, F.; Li, C.; Arrive, C.; Bertrand, M.; Brabec, C. J.; Egelhaaf, H. J. Fully Solution Processed Pure  $\alpha$ -Phase Formamidinium Lead Iodide Perovskite Solar Cells for Scalable Production in Ambient Condition. *Adv. Energy Mater.* **2020**, *10* (42), 1–11. <https://doi.org/10.1002/aenm.202001869>.
- (22) Du, M.; Zhu, X.; Wang, L.; Wang, H.; Feng, J.; Jiang, X.; Cao, Y.; Sun, Y.; Duan, L.; Jiao,

Y.; Wang, K.; Ren, X.; Yan, Z.; Pang, S.; Liu, S. High-Pressure Nitrogen-Extraction and Effective Passivation to Attain Highest Large-Area Perovskite Solar Module Efficiency. *Adv. Mater.* **2020**, *32* (47), 1–10. <https://doi.org/10.1002/adma.202004979>.

- (23) Bishop, J. E.; Read, C. D.; Smith, J. A.; Routledge, T. J.; Lidzey, D. G. Fully Spray-Coated Triple-Cation Perovskite Solar Cells. *Sci. Rep.* **2020**, *10* (1), 1–8. <https://doi.org/10.1038/s41598-020-63674-5>.
- (24) Chen, S.; Dai, X.; Xu, S.; Jiao, H.; Zhao, L.; Huang, J. Stabilizing Perovskite-Substrate Interfaces for High-Performance Perovskite Modules. *Science (80-. ).* **2021**, *373* (6557), 902 LP – 907. <https://doi.org/10.1126/science.abi6323>.
- (25) Feng, J.; Jiao, Y.; Wang, H.; Zhu, X.; Sun, Y.; Du, M.; Cao, Y.; Yang, D.; Liu, S. (Frank). High-Throughput Large-Area Vacuum Deposition for High-Performance Formamidine-Based Perovskite Solar Cells. *Energy Environ. Sci.* **2021**, *14* (5), 3035–3043. <https://doi.org/10.1039/d1ee00634g>.
- (26) Chen, S.; Xiao, X.; Gu, H.; Huang, J. Iodine Reduction for Reproducible and High-Performance Perovskite Solar Cells and Modules. **2021**, 1–7. <https://doi.org/10.1126/sciadv.abe8130>.
- (27) Adugna, G. B.; Abate, S. Y.; Wu, W. T.; Tao, Y. T. Toward Large-Area and Fully Solution-Sheared Perovskite Solar Cells. *ACS Appl. Mater. Interfaces* **2021**. <https://doi.org/10.1021/acsami.1c03460>.
- (28) Yang, F.; Dong, L.; Jang, D.; Saparov, B.; Tam, K. C.; Zhang, K.; Li, N.; Brabec, C. J.; Egelhaaf, H. J. Low Temperature Processed Fully Printed Efficient Planar Structure Carbon

Electrode Perovskite Solar Cells and Modules. *Adv. Energy Mater.* **2021**, *2101219*.  
<https://doi.org/10.1002/aenm.202101219>.

- (29) Seto, S. Inverted Planer Perovskite Solar Cells Fabricated by All Vapor Phase Process. *Jpn. J. Appl. Phys.* **2021**, *60*, 0–6. <https://doi.org/10.35848/1347-4065/abdad3>.